Natural Resources Research, Vol. 30, No. 3, June 2021 (© 2021)
https://doi.org/10.1007/s11053-021-09861-1

Original Paper

3D Multi-scale Reconstruction of Fractured Shale and Influence of Fracture Morphology on Shale Gas Flow

Peng Hou,[1,2,3,4] Xin Liang,[5,6] Yun Zhang,[1] Jian He,[3] Feng Gao,[3] and Jia Liu[5]

Received 18 December 2020; accepted 12 March 2021
Published online: 27 March 2021

Quantitative characterization of shale gas flow in fractured shale is a key problem in shale gas extraction. In this study, 3D multi-scale structures in fractured shale were reconstructed, firstly, by X-ray micro-computerized tomography (CT), high-resolution scanning electron microscope (SEM), and fractal function. Then, a REV (representative elementary volume)-scale lattice Boltzmann (LB) model, considering Klinkenberg's effect and gas absorption, was built, and the effects of fracture complexity and gas pressure on shale gas flow and shale permeability were analyzed and studied quantitatively. The simulation results indicate that the gas flow behaviors in the fractured shale are related strongly to fracture morphology and gas pressure. The decreased fracture fractal dimension or increased complexity of the fracture network leads to increase in permeability of the fractured shale. The gas velocity in the shale matrix decreases with increasing fracture roughness. Increased fracture network connectivity contributes to the formation of local high-intensity velocity fields and the improvement of gas flow in the shale matrix. The gas rarefaction effect has a significant influence on gas flow in the fractured shale, and permeability of the fractured shale must be regarded as a dynamic shale reservoir parameter. The gas flow behavior in the fractured shale is more sensitive at low-pressure condition whereas the gas rarefaction effect is more sensitive to the fractured shale with highly rough fracture or low fracture connectivity.

KEY WORDS: Fractured shale, Fractal fracture, Gas flow, Permeability, Lattice Boltzmann method.

INTRODUCTION

As a clean and efficient form of hydrogen energy, shale gas is expected to be an ideal alternative energy for conventional natural gas owning to its huge reserves (Nelson, 2009). Compared with conventional gas, shale gas is hard to extract due to low porosity and permeability of shale reservoir (Darabi et al., 2012; Tahmasebi et al., 2016; Li et al., 2020). So far, there are many effective stimulation methods to improve the permeability of shale reservoirs, such as hydraulic fracturing, liquid N_2 fracturing, and CO_2 fracturing (Guo et al., 2015; Hou, Gao, et al., 2017, 2018; Huang et al., 2019). By using effective stimulation methods, the fracture/fracture network is induced in shale matrix, and then a complex pore-fracture system is formed (Hou et al., 2018). The pore-fracture system provides main channels for shale gas flow, and it is a primary factor to control future shale gas production (Chen, Zhang, et al.,

---

[1] State Key Laboratory of Coal Resources in Western China, Xi'an University of Science and Technology, Xi'an 710054, Shaanxi Province, China.
[2] State Key Laboratory of Geohazard Prevention and Geoenvironment Protection, Chengdu University of Technology, Chengdu 610059, Sichuan Province, China.
[3] State Key Laboratory for Geomechanics and Deep Underground Engineering, China University of Mining and Technology, Xuzhou 221116, Jiangsu Province, China.
[4] IPPH, Purdue University, West Lafayette, IN 47907, USA.
[5] School of Civil Engineering and Architecture, Xi'an University of Technology, Xi'an 710048, Shaanxi Province, China.
[6] To whom correspondence should be addressed; e-mail: xliang@xaut.edu.cn

1520-7439/21/0600-2463/0 © 2021 International Association for Mathematical Geosciences

2015; Benamram et al., 2016; Hou et al., 2020). Therefore, quantitative characterization of fluid transport process in internal structure of fractured reservoir rocks is the key problem to shale gas extraction. Currently, seepage experiments have been employed widely to study permeability characteristics of rock, some macro-scale parameters can be obtained. However, fractured shale is like a "black box"; it is hard to know fluid flow behavior inside a rock based on seepage experiments (Wu et al., 2017). In such context, numerical simulation methods present a significant advantage. Because the pore-fracture structure of fractured shale is a typical multi-scale system, digital core reconstruction of fractured shale and multi-scale gas flow of pore-fracture system becomes the current research hotspot.

Real 3D digital cores can be directly constructed in different resolutions by modern imaging techniques, such as focused ion beam scanning electron microscope (FIB–SEM) (Dewers et al., 2012) and X-ray Computer Tomography (including industrial CT, micro-CT, and nano-CT) (Wang et al., 2019). Though high-resolution imaging of nano-scale pores in shale can be obtained by the FIB–SEM and nano-CT, it can only scan micro-scale volumes of shale, and the constructed volume of shale is too small to represent shale features (Ji et al., 2019). Industrial CT and micro-CT can obtain a larger field of view, but their resolutions are relatively low and the nano-scale information of shale is not reflected (Ji et al., 2019). Thus, a single modern imaging technique cannot satisfy the requirements of 3D core reconstruction of shale and a trade-off must be made between observing scale and resolution. To characterize the multi-scale pore structure of shale, different modern imaging techniques have been tried to be integrated. Tang et al. (2016) analyzed the characteristics of heterogeneous nano-porosity of the Silurian Longmaxi Formation shale through quantitative evaluation of minerals using scanning electronic microscopy (QEMSCAN), FIB–SEM, and nano-CT. Saif et al. (2017) studied the multi-scale microstructure imaging of oil shale pyrolysis using micro-CT, scanning electron microscope (SEM), modular automated processing system (MAPS) mineralogy and FIB–SEM. Wu et al. (2020) investigated the pores of the Wufeng–Longmaxi shale at different scales by combined use of micro-CT, SEM, FIB–SEM, and focused ion beam helium ion microscope (FIB–HIM). At present, most studies focus mainly on multi-scale characterization (ranging from nano-scale to micro-scale) of pore structures of shale matrix using high-resolution reconstruction technology. For fractured shale, current studies concentrate largely on the reconstruction and visualization of induced fractures using industrial CT and micro-CT, but pore structure is neglected (Jiang et al., 2019). The reconstruction of real pore-fracture structure in fractured shale is hardly possible due to the relatively large difference in scale levels between pores and induced fractures. Therefore, combining high-resolution and low-resolution methods is commonly used to analyse the multi-scale structure of fracture shale (Fig. 1) (Liu et al., 2018), but these two methods are carried out in parallel, and real pore-fracture structures have not been reconstructed. However, a real pore-fracture system is very important for the study of gas transport characteristics between pore space and fracture space. To overcome this limitation, modern imaging techniques and reconstruction algorithms were combined in this study. The representative elementary volume (REV) of shale matrix was reconstructed using micro-CT and high-resolution SEM, and 3D fractures were generated in the REV of shale matrix by using a 3D fractal function because the crack morphology of fractured rock is generally considered to have fractal characteristics (Ju et al., 2017).

Gas flow in porous media can be generally classified into three kinds: pore-scale, REV-scale, and domain-scale (Guo & Zhao, 2002). Compared with pore-scale models, REV-scale models of porous flow characteristics can be controlled and have higher computational efficiency because detailed features of pore structures are ignored (Guo & Zhao, 2002). Therefore, multiple REV-scale models have been proposed to numerically model fluid flow, such as the extended Darcy models and generalized model based on the generalized Navier–Stokes (N–S) equations. The lattice Boltzmann method (LBM) (Zhang et al., 2019), as an alternative and efficient method for simulating fluid flow, has been employed widely to model fluid dynamics in porous media due to its obvious advantages over conventional numerical methods, such as good numerical stability, natural parallelism, simple fluid–solid boundary (Chen et al., 2014; Hou, Ju, et al., 2017). So far, significant efforts have been made in this area, and some REV-scale LBM models have been reported. Guo and Zhao (2002) proposed a generalized REV-scale lattice Boltzmann (LB) model for incompressible flow in porous media, and this model can

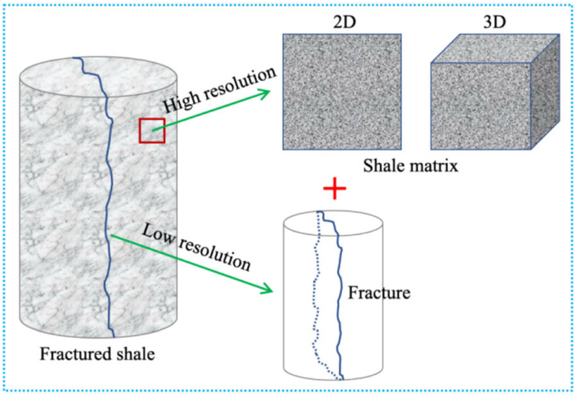

Figure 1. Schematic diagram of current multi-scale analysis of fractured shale.

recover the generalized N–S equations in the incompressible case. Then, Chen, Kang, et al. (2015) established a REV-scale LB model of porous medium considering Klinkenberg's effect, and found that the Klinkenberg's effect plays an important role in gas flow in tight porous media. Because, in the REV-scale LBM model, the detailed spatial distribution of the pore structure of shale is represented by macroscopic physical parameters, such as porosity and permeability, this method can solve well the multi-scale flow problem in a pore-fracture structure. Chen, Fang, et al. (2015) studied gas flow in 2D porous media with a tree-like fracture based on the REV-scale LBM model. Ren et al. (2019) investigated the effects of multiple mechanisms on gas flow in 2D tight porous media with a smooth fracture by using the REV-scale LBM model; however, fractures in their porous media are relatively arbitrary and simple. In fact, the fracture morphology in fractured shale is extremely complex (Jiang et al., 2019), and it has an obvious influence on gas transport (Miao et al., 2015). It should be noted that above studies were performed in 2D conditions, which result in different permeability compared to 3D porous media (Cai et al., 2018). Moreover, gas adsorption also plays an important role in gas transport due to high organic matter content in shale (Shen et al., 2018; Hou et al., 2020), and so it should be also considered in the REV-scale LBM model.

In this study, the high-resolution SEM system and X-ray micro-CT were applied to analyse and reconstruct the 3D matrix structure of shale with multi-scale and multi-component. The 3D fracture with fractal characteristics was used to represent the fracture induced by effective stimulation methods, and it was embedded into the 3D reconstructed shale matrix. Then, a REV-scale LB model was developed to analyse the gas flow mechanism in fractured shale with consideration of Klinkenberg's effect and gas absorption. Gas flow behaviors under different fracture complexities and different pore pressures were studied and visualized.

3D RECONSTRUCTION OF FRACTURED SHALE

Shale Matrix and Its Representative Elementary Volume

Shale samples obtained from the Longmaxi Formation at Shizhu country, Chongqing city, China were used as the experimental materials. Although most pores in shale are distributed at the nano level, the sizes of mineral particles in shale were in the range of 3.2–3.5 μm (Lei et al., 2015). In order to meet the observation field size and ensure the accuracy of internal structure characterization, 2D and 3D modern imaging techniques were combined (Fig. 2a). Firstly, micro-CT was used to reconstruct mineral components and pores between mineral particles in shale. Then, the pore distribution of various mineral components in shale was observed by a high-resolution SEM. In this way, the large-scale and high-precision structure of shale can be reconstructed by a multi-component and multi-scale method.

In the 3D modern reconstruction, the high-resolution 3D X-ray microscopic imaging system Xradia 510 Versa (see Fig. 2d), as a micro-CT, was employed to reconstruct the shale matrix. Its highest resolution in 3D space can reach 500 nm. A cylindrical shale specimen with a diameter of 2 mm was processed, and the resolution of the micro-CT 2 μm was set in the test. Because shale is composed mainly of organic matter and inorganic matter, the shale matrix was divided into organic matter, inter-granular pore, and inorganic matter based on the gray value of the images during the component segmentation.

To describe accurately the internal structure of shale, the selection of the sample size is very important because of the heterogeneity of shale. In theory, the larger size of the sample, the high accuracy; however, the larger size of a sample, the higher the requirement for computing of related numerical calculations. To take account of both calculation efficiency and accuracy of the research results, the REV, which is usually involved in geosciences, was adopted in this study. The REV extraction process was as follows.

1. Select any point near the core location and take it as the center; then, select a cube with a set edge length to count its porosity and effective porosity.
2. Expand gradually the cube edge length, and calculate the contribution ratio of organic matter, inter-granular pores, and inorganic matter for each selected cube one by one.
3. Select different centers and repeat steps 1 and 2.
4. Draw the curve of the contribution ratio of three components varying with the cube edge length.

The corresponding minimum size is the size of the REV when all of them are stable. The relative gradient error $\varepsilon_g = \left|(n^{n+1} - n^{n-1})/(n^{n+1} + n^{n-1})\right|/\zeta$ was employed to judge the stability of the contribution ratio (Costanza-Robinson et al., 2011), where i is the window increment number, n is the contribution ratio of each shale component, ζ is the magnitude of increment in the side length. The stability of the contribution ratio was estimated using the $\varepsilon_g<0.2$. In this study, three different centers were selected, and a Matlab program was compiled according to the above-mentioned steps for acquisition of the REV. The contribution ratios of organic matter, inter-granular pores, and inorganic matter in shale under the different cube sizes are shown in Figure 3. As can be seen from the figure, the REV size of the shale was 250 × 250 × 250 (2 μm), and the 3D REV structure is shown in Figure 4a.

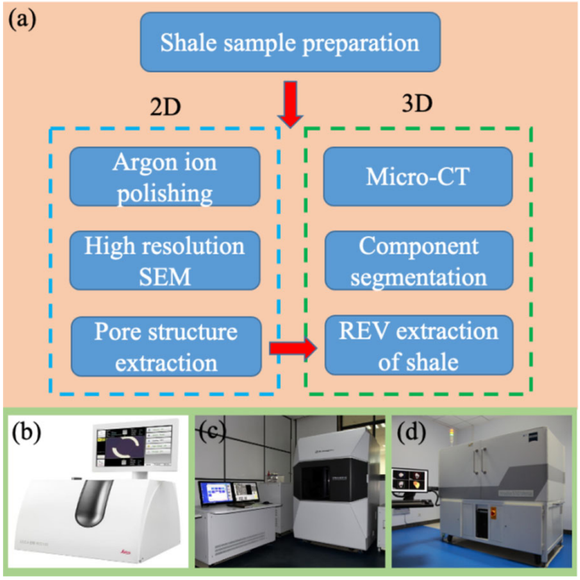

Figure 2. Reconstructed flow-chart of shale matrix and facilities: (a) reconstructed diagram of shale matrix; (b) Argon-ion polisher; (c) electron probe micro-analyzer, and (d) micro-CT.

After segmentation and extraction, the distribution of organic matter and inter-granular pores is shown in Figure 4b, c, respectively. The proportions of organic matter, inter-granular pore, and inorganic matter in the shale characterization units were 17.95%, 3.29%, and 78.76%, respectively. The connectivity of inter-granular pores was very poor, and most of them were isolated, which reveals why the shale has ultra-low permeability. The pore width distribution of the inter-granular pore is shown in Figure 4d. The pore diameter of inter-granular pores was distributed mainly in the range of 6–16 μm, in which the pore diameter of 7 μm was the most frequent.

Characteristics of Nanometer Pore

In modern 2D imaging experiments, the surface of a shale sample is polished firstly by using the argon-ion polisher LEICA EM RES102 (Fig. 2b). Then, the electron probe microanalyzer EPMA-8050G (Fig. 2c) is employed to observe the pore structure in the organic matter and inorganic matter. The secondary electron image resolution of the EPMA-8050G can reach 3 nm, and the maximum magnification of the sample can be 400,000 times. Subsequently, in this study, the SEM images were segmented based on the gray value. Pore structures in the organic and inorganic matter were extracted (Fig. 5). To ensure the accuracy of the data, three different areas were selected and analyzed by the same process.

Through the above statistical analysis, the porosity in the organic and inorganic matter is summarized in Table 1. From this table, the average porosities of organic matter and inorganic matter in shale were 14.07% and 3.41%, respectively. The porosity of organic matter was 4.13 times greater than that of inorganic matter, which reflects that organic matter in shale can preserve more shale gas.

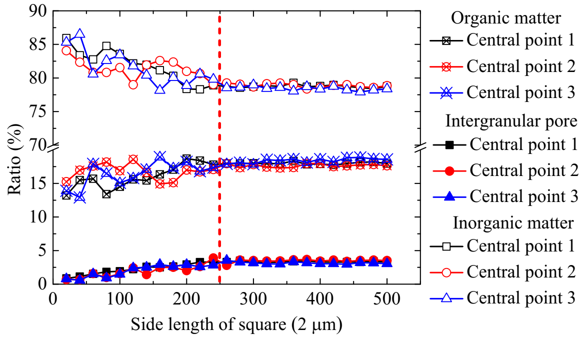

Figure 3. Change in ratio of shale components with size of extraction structure.

Fractal Reconstruction of 3D Fracture

The 3D structure of the shale matrix has been reconstructed in the above section. However, after the effective external stimulation for shale reservoirs, single fracture or fracture networks can be generated. Due to the irregular shape of the cracks, these cracks serve as the main channels for fluid migration, and their morphological characteristics have an important impact on fluid migration. Quantitative analysis and description of the fluid seepage mechanism in fractured shale have become a difficult and hot topic. In many reported literatures (e.g., Li et al., 2016a; Jia et al., 2018), the fracture induced by hydraulic fracturing has fractal characteristics. Therefore, in this study, the Weierstrass–Mandelbrot fractal function was employed to model the different fracture morphology, in which 3D space can be expressed as (Ausloos & Berman, 1985):

$$z(x,y) = L\left(\frac{G_0}{L}\right)^{(D-2)}\left(\frac{\ln b}{M}\right)^{1/2}\sum_{m=1}^{M}\sum_{n=0}^{n_{\max}} b^{(D-3)n} \times \left\{\cos\phi_{m,n} - \cos\left[\frac{2\pi b^{n}\left(x^2+y^2\right)^{1/2}}{L}\cos\left(\tan^{-1}\left(\frac{y}{x}\right)-\frac{\pi m}{M}\right)+\phi_{m,n}\right]\right\} \tag{1}$$

where D is the fractal dimension ($2 \le D < 3$); G_0 is fractal roughness; l is sample size; M_0 is the superposition ridge number, and its value is 20 in this paper; and $\phi_{m,n}$ is the random phase angle, and the range of its values is 0–2π.

Based on the Weierstrass–Mandelbrot fractal function, nine different fractured shales were reconstructed and shown in Figure 6. In this figure, the symbols N and D represent fracture number and fracture fractal dimension, respectively. The width of all reconstructed fractures was 16 pixels. Figure 6a displays that a single fracture was added to the reconstructed REV of the shale, and their fracture fractal dimensions were 2.0, 2.1, 2.2, 2.3, 2.4, and 2.5, respectively. The reconstructed fracture networks are presented in Figure 6b. To simplify the comparative study, the fractal dimension of every fracture was set as 2.3 in these systems.

Through statistical analysis, the characteristic parameters of the reconstructed pore-fracture structures of shale are summarized in Table 2. The inorganic matter has the largest proportion among the three components. The proportion of the pore-fracture increased slightly with increasing fracture fractal dimension while it had a rapid increase with increasing fracture number. The proportion of pore-fracture is larger than that of organic matter when the fracture number was more than 3.

GAS TRANSPORT MODEL FOR 3D REV

Generalized N–S Model and Darcy's Modification

Based on the generalized N–S equation proposed by Nithiarasu et al. (1997), the incompressible isothermal fluid transported in a REV can be described as:

$$\nabla \cdot (u) = 0 \tag{2}$$

$$\partial_t(u) + (u \cdot \nabla)\frac{u}{\phi} = -\frac{1}{\rho}\nabla(\phi p) + \upsilon_e \nabla^2(u) + F_b \tag{3}$$

where u is the fluid velocity vector, p is fluid pressure, ρ is fluid density, ϕ is porosity, υ_e is effective viscosity, and it can be calculated as $\upsilon_e = \upsilon J$, υ is shear viscosity, and J is the ratio of viscosity. F_b is the total force, which includes the internal force caused by the pore medium and the external force; it can be expressed as:

$$F_b = -\frac{\phi\upsilon}{K}u - \frac{\phi F_\phi}{\sqrt{K}}|u|u + \phi G \tag{4}$$

where G is the external physical force, K is permeability, and F_ϕ is the geometric function. The first term in the right-hand side of Eq. 4 is the linear Darcy drag force, the second term is the nonlinear towing force, and the third term is the total external force. For porous media with extremely low per-

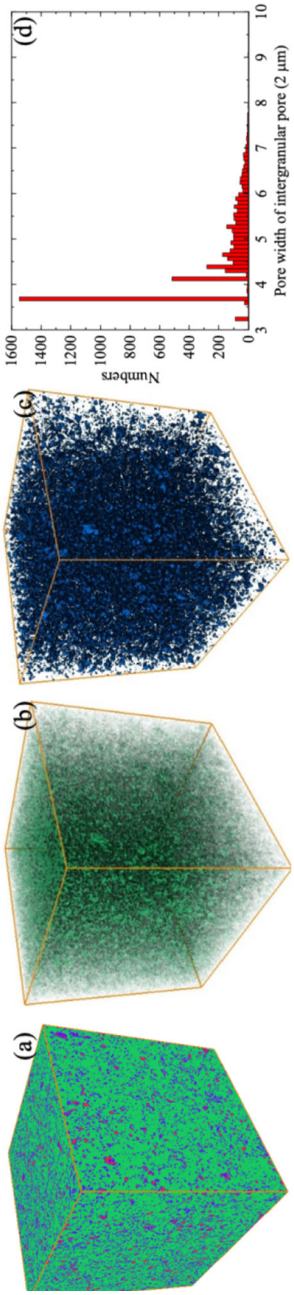

Figure 4. REV of shale and distribution of organic matter and inter-granular pore: (a) REV of shale; (b) organic matter; (c) inter-granular pore, and (d) pore width distribution of inter-granular pore.

meability, the velocity of fluid is ultra-low, and an ultra-low nonlinear drag force is induced (Javadpour et al., 2007). Therefore, the second term in the right-hand side of Eq. 4 can be ignored, and the expression of the total force can be simplified as:

$$F_b = -\frac{\phi \upsilon}{K} u + \phi G \tag{5}$$

When the mean free path (MFP) of the molecule is close to the characteristic length of a domain, a slippage effect can be observed near the solid wall. Klinkenberg (1941) was the first to study the phenomenon of gas slippage in porous media and proposed a linear relationship to correct gas permeability. The modified expression is:

$$k_{\mathrm{a}} = f_{\mathrm{c}} k_{\mathrm{d}} \tag{6}$$

where k_{a} and k_{d} are the apparent permeability and intrinsic permeability, respectively; their values are related only to the internal pore space distribution of the pore medium and are not affected by external conditions. f_{c} is the correction factor. There are many kinds of expressions for the correction factor. In this research, the second-order relations proposed by Beskok and Karniadakis (1999) were selected to describe the whole four flow regimes defined according to Knudsen number (Kn), thus:

$$f_{\mathrm{c}} = (1 + \alpha(Kn)Kn)\left(1 + \frac{4Kn}{1 - b' Kn}\right) \tag{7}$$

where b' is the slip coefficient, and its value is equal to -1 when gas flow shows a slip phenomenon. $\alpha(Kn)$ is a rarefaction effect coefficient of gas, which can be expressed as (Civan, 2010):

$$\alpha(Kn) = \frac{1.358}{1 + 0.170 Kn^{-0.4348}} \tag{8}$$

It can be seen from the above equations that the value of the Knudsen number needs to be calculated. According to its definition, its value can be determined by the ratio of the MFP and the characteristic pore diameter of the pore medium. The MFP can be given by Chen, Fang, et al. (2015):

$$\lambda = \frac{\mu}{p} \sqrt{\frac{\pi R T}{2M}} \tag{9}$$

where T is temperature, R is the gas constant, M is the gas molar mass, and μ is the dynamic viscosity.

According to Heid et al. (1950), the characteristic pore size r_d of porous media can be obtained as:

$$r_d = 8.886 \times 10^{-2}\sqrt{\frac{k_d}{\phi}} \tag{10}$$

where the intrinsic permeability of pore media can be obtained with the Kozeny–Carman (KC) equation (Carman, 1997), thus:

$$k_d = C_0\frac{\phi^3}{(1-\phi)^2} \tag{11}$$

where C_0 is the KC constant. For a stacking balls model, its value is equal to $d_s^2/150$, and d_s is the diameter of the stacking balls.

Besides, a gas adsorption layer exists on the walls of organic pores. According to results of molecular dynamic (MD) simulations by previous researches (e.g., Li et al., 2016b; Hou et al., 2020), the thickness of the adsorption layer depends on gas pressure, and so the thickness of the gas adsorption layer can be obtained as:

$$\delta = \frac{p-p_1}{p_2-p_1}(\delta_2-\delta_1) \tag{12}$$

where δ_1 and δ_2 are the thicknesses of the adsorption layer at pressures p_1 and p_2, respectively. The thicknesses of gas absorption layer are 0.4 nm and 0.6 nm at gas pressures of 5 MPa and 20 MPa, respectively (Hou et al., 2020). Therefore, the characteristic size of pore in organic matter can be modified with $r_d - \delta$.

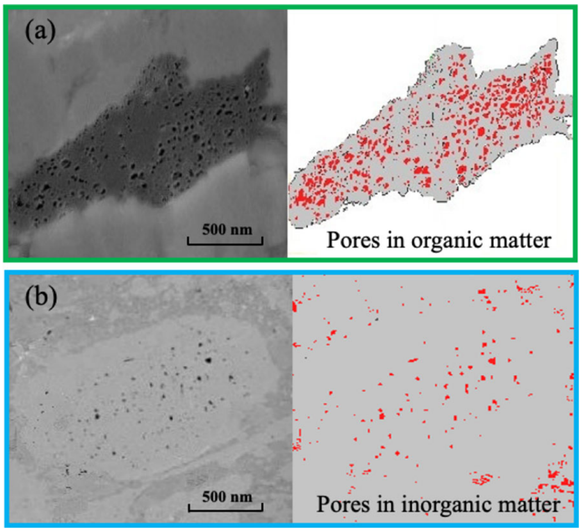

Figure 5. Pore structure in the shale sample's (a) organic matter and (b) inorganic matter.

Taking methane as an example, Figure 7 shows the relationships of the Knudsen number, pore size, correction factor, and porosity. The required parameters for the calculation were set as $d_s = 30\,\text{nm}$, $M = 0.016\,\text{kg}\,\text{mol}^{-1}$, $T = 313\,\text{K}$. Four different pressures (1 MPa, 5 MPa, 10 MPa, and 20 MPa) were selected to analyse their influence on the Knudsen number. The viscosity of methane corresponding to various pressures was obtained through the Peace online software. From the figure, it can be seen that the pore diameter was less than 10 nm when the porosity was less than 0.34, which is consistent with the characteristic of shale pore structure. With decrease in porosity, the Knudsen number increased nonlinearly. The lower the gas pressure, the larger the Knudsen number. As porosity decreased further, the Knudsen number was in the range from 0.1 to 10, which indicates that the gas flow presents a transition flow region. Besides, the correction coefficient also increased nonlinearly with decrease in porosity, which is similar to the variation of the relationship between the Knudsen number and porosity. At the same time, the correction coefficient reached a maximum value of 52 when the gas pressure was 1 MPa. However, the maximum value of the correction coefficient was only 3 at gas pressure of 20 MPa. The results indicate that the gas pressure plays a key role in the micro-scale flow field.

Table 1. Porosity in organic matter and inorganic matter of shale.

Component	Porosity (%)			
	Sample 1	Sample 2	Sample 3	Mean value
Organic matter	15.28	12.75	14.19	14.07
Inorganic matter	2.81	4.34	3.07	3.41

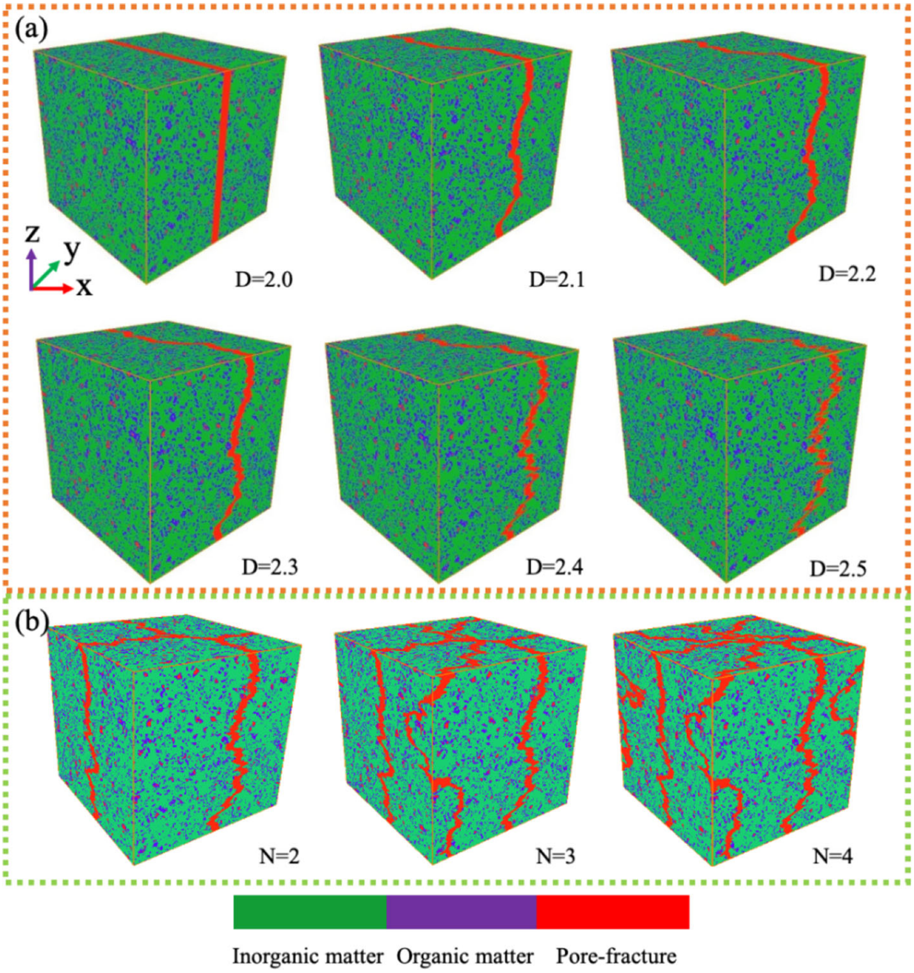

Figure 6. Reconstructed pore-crack structure of shale: (a) single fracture and (b) multi-fractures.

Table 2. Basic parameters in reconstructed pore-crack structure of shale.

Parameter	Fractal dimension of fracture						Fracture number		
	2.0	2.1	2.2	2.3	2.4	2.5	2	3	4
Pore-fracture (%)	7.40	7.41	7.48	7.45	7.53	7.66	14.00	19.88	25.34
Organic matter (%)	17.16	17.16	17.12	17.13	17.07	17.02	16.33	15.22	14.17
Inorganic matter (%)	75.44	75.43	75.40	75.42	75.40	75.32	69.67	64.90	60.49

REV-Scale LBM Model

The pore size of shale matrix was in nanoscale, and the connectivity of pores was extremely poor. The induced fracture was generally larger than the micro-scale, and so the fractured shale is a typical multi-scale system. Thus, the pore-scale LB model is hard to deal in the multi-scale problem due to the huge demand for computational resource. However, the REV-scale LB model does not require paying attention to the details of gas flow inside real pores, and it provides an effective way to solve the multi-

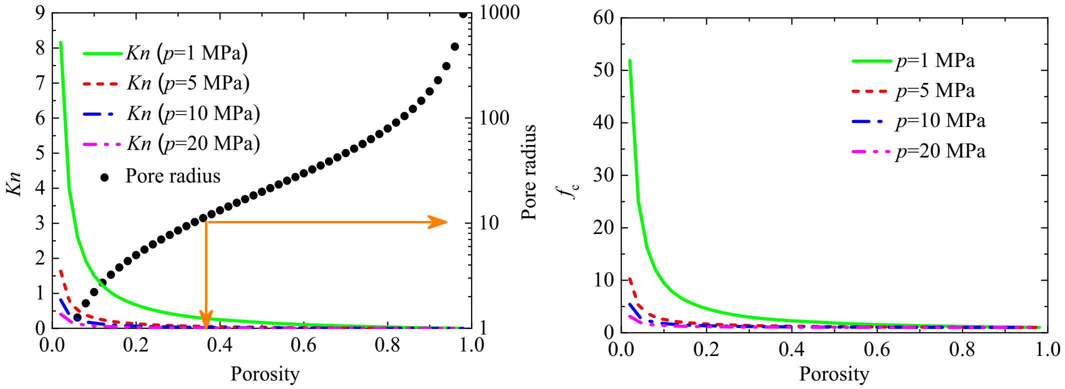

Figure 7. Effect of porosity on Knudsen number, pore radius, and correction factor.

scale problem. In the REV-scale LB model, it is only necessary to input the basic statistical parameters of shale, such as porosity and permeability that can be obtained by experimental methods or theoretical models.

In this study, a 3D REV-scale LB model was developed to solve the above generalized N–S equations for gas flow with Klinkenberg's effect and gas absorption in tight porous media based on the work of Guo and Zhao (2002). The governing equation of the density distribution can be expressed as:

$$f_{\sigma,i}(x+e_i\Delta t, t+\Delta t) - f_{\sigma,i}(x,t) = -\frac{1}{\tau_{\sigma,v}}\left[f_{\sigma,i}(x,t) - f^{\mathrm{eq}}_{\sigma,i}(x,t)\right] + \Delta t F_{\sigma,i} \qquad (13)$$

where $f_{\sigma,i}(x,t)$ is the distribution function at the lattice site $\mathbf{x}$ and time t, $f^{\mathrm{eq}}_{\sigma,i}$ is the equilibrium distribution function of i direction, F_i is the discrete distribution function of the external force term, $c = \Delta x/\Delta t$ is the lattice speed with Δx and Δt as the lattice spacing and time step, respectively, and τ is the dimensionless relaxation time. The subscript σ represents the different components. When its value is equal to 1, it represents the component of pore-crack, 2 for inorganic matter, and 3 for organic matter. To balance the computational speed and the accuracy of the results (Bauer & Rüde, 2018), a D3Q19 was used for the lattice model in this simulation, and the discrete lattice velocity $\mathbf{e}_i$ is given by:

$$e_i = \begin{bmatrix} 0 & 1 & -1 & 0 & 0 & 0 & 0 & 1 & -1 & 1 & -1 & 1 & -1 & -1 & 1 & 0 & 0 & 0 & 0 \\ 0 & 0 & 0 & 1 & -1 & 0 & 0 & 1 & -1 & -1 & 1 & 0 & 0 & 0 & 0 & 1 & -1 & 1 & -1 \\ 0 & 0 & 0 & 0 & 0 & 1 & -1 & 0 & 0 & 0 & 0 & 1 & -1 & 1 & -1 & 1 & -1 & -1 & 1 \end{bmatrix} \qquad (14)$$

To consider the local porosity of each component in the model, the equilibrium distribution function can be modified as:

$$f^{\boldsymbol{eq}}_{\sigma,i} = w_i\rho_\sigma\left[1 + 3\frac{e_i \cdot u_\sigma}{c^2} + \frac{9}{2}\frac{(e_i \cdot u_\sigma)^2}{\phi_\sigma c^4} - \frac{3}{2}\frac{u_\sigma \cdot u_\sigma}{\phi_\sigma c^2}\right] \qquad (15)$$

where ϕ_σ represents the porosity of different components, and the weight factors ω_i are given by:

$$\omega_i = \begin{cases} 1/3 & e_i^2 = 0 \\ 1/18, & e_i^2 = 1 \\ 1/36, & e_i^2 = 2 \end{cases} \qquad (16)$$

For the term $F_{\sigma,i}$ in Eq. 13, the gravity of the gas was ignored in this study. Therefore, the force in this model mainly refers to the total force F_b. Based on the external force scheme proposed by Guo et al.

(2002), the local porosity of three different components can be considered as:

$$F_{\sigma,i} = w_i\rho_\sigma\left(1-\frac{1}{2\tau}\right)\left[3\frac{e_i\cdot F_{\sigma,\mathrm{b}}}{c_s^2}+9\frac{(e_i\cdot u_\sigma)(e_i\cdot F_{\sigma,\mathrm{b}})}{\phi_\sigma c_s^4}-3\frac{u_\sigma}{}\right. \tag{17}$$

Similarly, the macroscopic density ρ_σ and velocity u_σ of the gas in each component were, respectively:

$$\rho_\sigma = \sum_i f_{\sigma,i} \tag{18}$$

$$\rho_\sigma u_\sigma = \sum_i f_{\sigma,i}e_i + \frac{\Delta t}{2}\rho_\sigma F_{\sigma,\mathrm{b}} \tag{19}$$

By combining Eqs. 5 and 19, the macroscopic velocity of the gas in each component can be obtained as:

$$u_\sigma = \frac{\sum_i f_{\sigma,i}e_i + \frac{\Delta t}{2}\rho_\sigma\phi_\sigma G_\sigma}{\rho_\sigma + \frac{\Delta t}{2}\frac{\phi_\sigma v}{k_{\sigma,a}}\rho_\sigma} \tag{20}$$

It can be seen from the above equation that the REV-scale LB model is very similar to the pore-scale LB model. When porosity is equal to 1, the REV-scale LB model is the same as the pore-scale LB model. In the REV-scale LB model, the continuous boundary is automatically satisfied in the interfaces between different components, which greatly reduces the computational cost and has the advantage to run simulations of large-scale geometric models.

Model Validation

To verify the effectiveness of the REV-scale LB model, the flow of one-component gas in the 2D model was simulated firstly. A porous medium with porosity of ϕ was filled into the two parallel plates. Gas flows from the left inlet to the right outlet. A pressure boundary was applied at the inlet and outlet boundary. The gas flow was driven by the pressure difference between the inlet and outlet. In this model, the gas flow can be described by the Brinkman-extended Darcy equation (Gao et al., 2014), thus:

$$\frac{v_e}{\phi}\frac{\partial^2 u}{\partial y^2} - \frac{v}{K}u + G = 0 \tag{21}$$

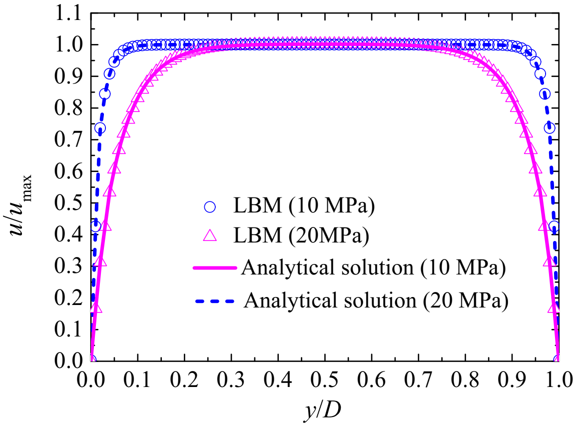

Figure 8. Comparison of velocity profiles between LB model simulation and analytical solution.

The non-slip boundary $u(x,0)=u(x,D)=0$ was employed on the upper and lower boundaries, where the direction of the x-axis was the same as the direction of gas flow; D is the distance between the two parallel plates, and G is the external force. By solving Eq. 21, the analytical solution of fluid velocity can be obtained as:

$$u = \frac{GK}{v}\left(1-\frac{\cosh[a(y-H/2)]}{\cosh(ah/2)}\right),\quad a=\sqrt{\frac{v\phi}{v_e K}} \tag{22}$$

where $\cosh(\zeta) = \left(e^{\zeta}+e^{-\zeta}\right)/2$, and G can be obtained by pressure difference $G=\Delta p/(L\rho)$, and L is the length of the plate in the x-direction. In addition, a hypothesis was made as follows: $v_e = v$.

Based on the above model, the simulation results and analytical solutions of the gas flow velocity between two parallel plates are shown in Figure 8. In the LB model, the gas adsorption was ignored. The size of the model was 200 × 100. The upper and lower plate walls were set as the non-slip boundary. The porosity was set to 0.5. Two gas pressures (10 MPa and 20 MPa) were set in this model. It can be seen that the simulation results of the LB model were consistent with the analytical solutions indicating that the established model is effective. At the same time, this model also can characterize the influence of Klinkenberg's effect on the gas flow. The smaller the gas pressure, the thicker the boundary layer.

To further verify the reliability of this model, the LB model was used to calculate the permeability of the 3D reconstructed shale matrix, and then calculated values were compared with the results of the experiments. Due to the low permeability characteristics of the shale, conventional seepage testing methods were not valid. Therefore, the seepage experiments were completed by using the PDP-200, which is a pulse attenuation gas seepage measurement system. The lowest permeability measured by the PDP-200 is 0.00001 mD.[1] The shale core size used in the gas seepage experiment was $\Phi 25 \times 50$ mm, and the reconstructed REV of the shale matrix was employed in the LB simulation. Five different outlet pressures (1, 2, 3, 4, and 5 MPa) were set in the LBM simulations and gas seepage experiments. In the LB model simulations, the inlet and outlet were set on the top and bottom of the core, respectively. The pressure boundary was applied to the inlet and outlet through the non-equilibrium extrapolation boundary condition. A periodic boundary was applied to the front, back, right, and left sides of the 3D geometric model. A pressure gradient of 0.1 MPa/m between the inlet and outlet was set. The temperature was set to 298.15 K. The porosities of the shale organic matter, inorganic matter, and inter-granular pore were set as 0.1407, 0.0341, and 1.0, respectively. The convergence criterion in the simulation was established based on the standard deviation of average energy. The simulation stopped when the mean energy standard deviation of the last two times was less than 10^{-6}. The shale permeability obtained by LB model simulation and seepage experiment is shown in Figure 9.

It can be seen from Figure 9 that the results obtained from the LB model simulations and experiments were close, but the permeability of the shale in the LBM simulations was generally larger than that in the experiments. This error was induced mainly by the existence of gas flow in the isolated pore in the LBM simulations. However, the deviation was smaller than 20%, indicating that the established model still can be used effectively to describe the permeability of the shale.

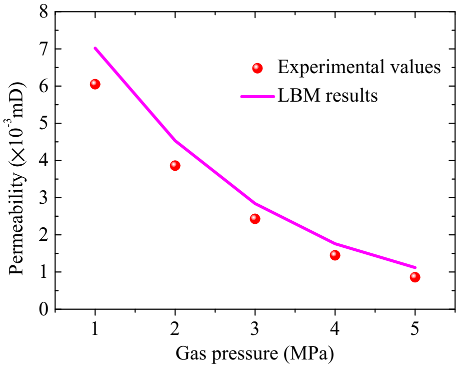

Figure 9. Comparison of shale permeability between LB model simulation and permeability test.

SIMULATION RESULTS

Fracture Roughness

In this section, the influence of the single fracture roughness on gas flow is studied. In the LBM simulation, the inlet and outlet of the core were set at the top and bottom, respectively. The pressure of the outlet was fixed at 5 MPa, and the pressure gradient between the inlet and outlet was set as 0.1 MPa/m. The porosity of the fracture and inter-granular pores was 1.0. The other settings were the same as the validation section. The 3D velocity distribution of gas flow was obtained and shown in Figure 10.

It can be seen in Figure 10 that the main flow path of gas was located inside the crack. The gas velocity in the shale matrix that was near the fracture wall had a significant increase due to the gas seepage from the induced crack. With increase in fractal dimension of the fracture, the gas velocity decreased obviously. The larger the fractal dimension of the fracture was, the rougher the fracture surface was, and the greater the gas flow resistance was. The gas velocity in other components was much smaller than that in the crack, while the gas velocity in the inter-granular pores was larger than that in the organic and inorganic matter. Compared with fracture, the seepage resistance in the shale matrix was greater, so that the gas was more likely to migrate in the fracture channel. It is impossible to characterize visually the gas seepage state in the shale matrix in Figure 10 because the gas velocity in the fracture was relatively large. Therefore, a 2D slice of the shale matrix (y = 200 μm) that was near the fracture wall in the fractured shale was ex-

---

[1] 1 mD (millidarcy) = 9.869233×10^{-13} m^2.

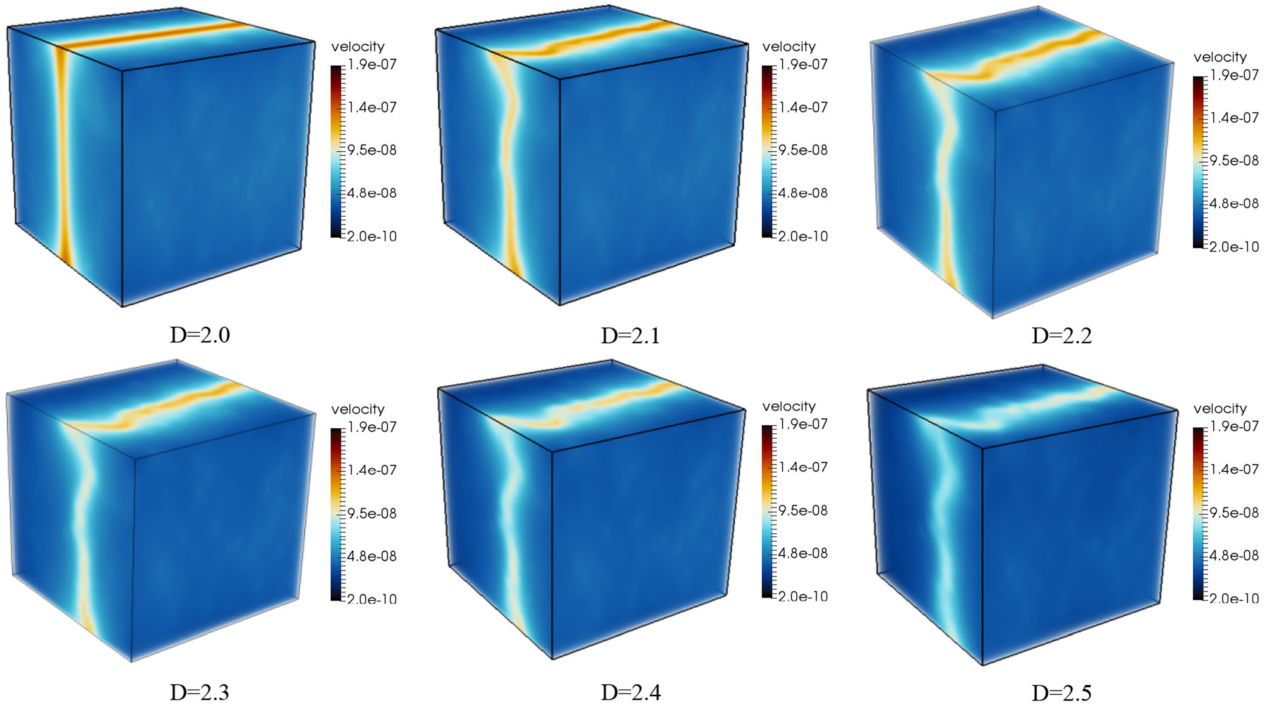

D=2.0 D=2.1 D=2.2

D=2.3 D=2.4 D=2.5

Figure 10. Velocity distribution in shale with single fracture.

tracted, and the gas velocity distribution in the extracted structure is shown in Figure 11. It can be seen that gas velocity in the shale matrix was almost 10 times lower than that in the fracture. The fracture fractal dimension also had an obvious influence on gas velocity in the shale matrix, and gas velocity in the shale matrix decreased with increase in fracture fractal dimension owing to the influence on gas velocity in the fracture space.

Based on Darcy's law and gas velocity in each component of the fractured shale, the permeability of the fractured shale can be calculated. The enhancement ratio of permeability is defined as the ratio of the permeability of the fractured shale to the permeability of the raw shale. Figure 12 displays the change in permeability of the fractured shale with fracture fractal dimension. As can be seen in the figure, the permeability of the fractured shale and the enhancement ratio of permeability both decreased significantly with increasing fracture fractal dimension. The permeability was reduced from 0.24 mD in the fractal dimension 2.0–0.18 mD in the fractal dimension 2.5. This reduction was 25%, but the minimum enhancement ratio of permeability still reached 270, which will be a great achievement for effective extraction of shale gas from low permeability shale reservoirs.

Complexity of Fracture Network

Gas flow in the fractured shale with different fracture networks was simulated. The fracture number was used to denote the complexity of the fracture network in this study. With increase in fracture number, the fracture network became more complex, and the intersections of the fractures also increased. The parameters and settings in the simulations were kept the same as in the previous section.

Figure 13 presents the gas velocity distribution in the fractured shale with different fracture numbers. As shown in the figure, gas velocity increased gradually with increase in the complexity of the fracture network, and this increasing trend was especially obvious at the intersection of the cracks. At the same time, the specific surface area of cracks increased rapidly with increase in fracture numbers, which resulted in much more pores being connected with the fracture wall and the gas velocity around the fractures also increased significantly. To clearly display the gas velocity distribution in the fractured

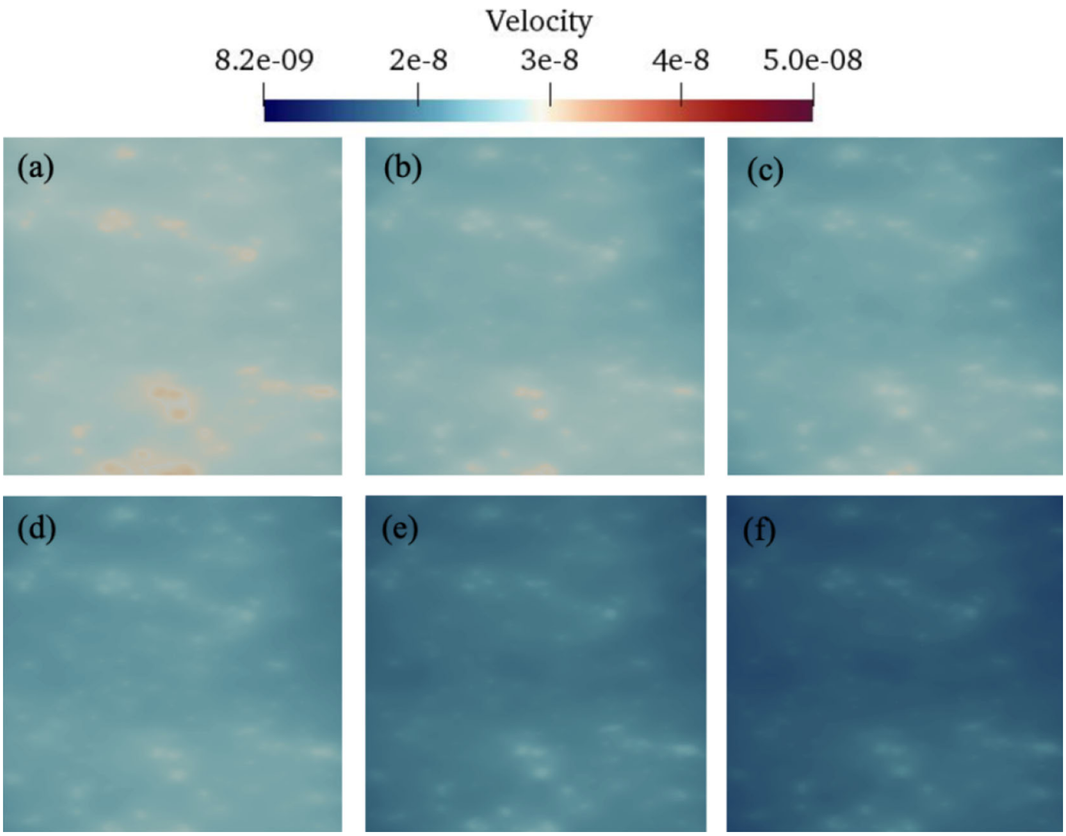

Figure 11. Effect of fracture fractal dimension on gas velocity distribution in the shale matrix, (a)–(f): 2.0, 2.1, 2.2, 2.3, 2.4, 2.5.

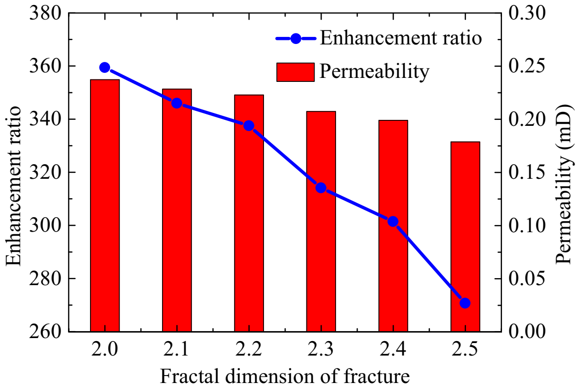

Figure 12. Effect of fracture fractal dimension on shale permeability.

shale and accurately analyse the influence of the fracture network complexity on the gas flow law, the central slice perpendicular (z = 250 μm) to the gas flow direction in the 3D velocity distribution field was extracted and presented in Figure 14. It can be seen from the figure that the more the fracture numbers were, the more the fracture intersection regions were formed, resulting in the increasing number of local high-intensity velocity fields. The good connectivity between the fractures can reduce resistance to gas flow and be more likely to decrease the probability of collision between internal gas molecules in the fracture wall, resulting in the increase of macroscopic gas velocity in the fracture.

The influence of the complexity of fracture network on permeability and permeability improvement ratio of the shale is shown in Figure 15. With increase in fracture numbers, the permeability and permeability improvement ratio of the fractured shale increased linearly. Compared with the shale with single fracture, the permeability improvement ratio of the shale with four fractures was increased by 194.57%, where the permeability and permeability enhancement ratio of the shale reached 0.61 mD and 925, respectively. The high

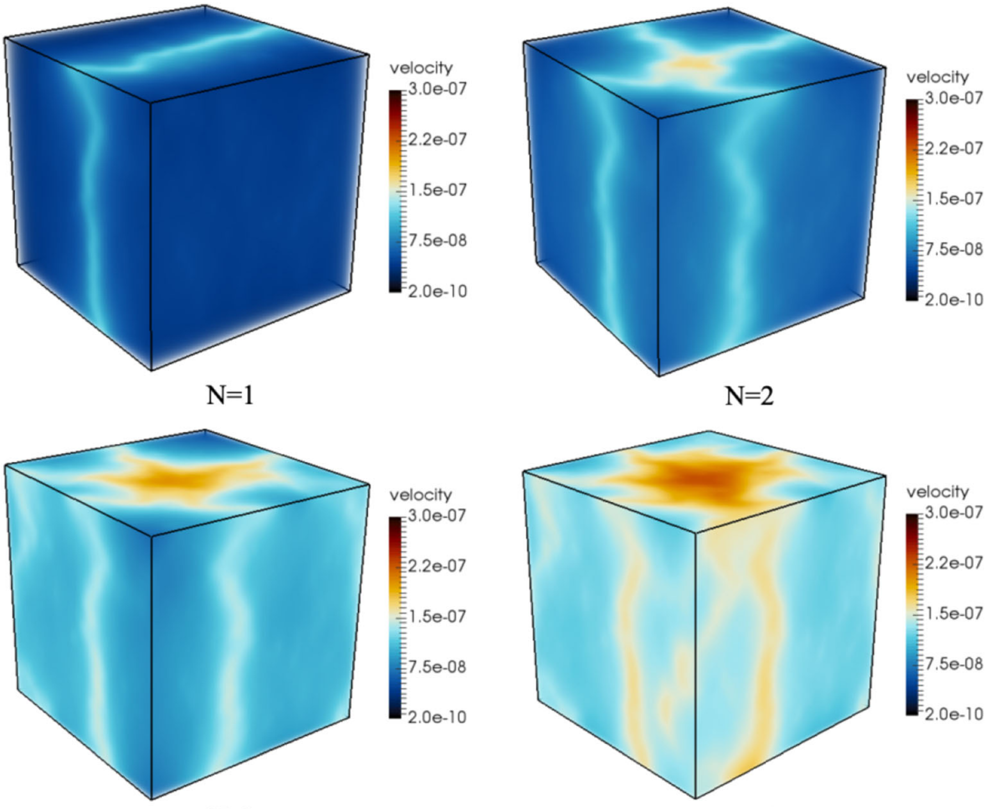

N=1 N=2

N=3 N=4

Figure 13. Velocity distribution in shale with different fracture numbers.

connectivity fracture network was conducive to reduction of resistance of gas transport and increase of gas flow passages. As a result, the more complex the fracture network was, the more obvious enhancement in the permeability was.

Gas Pressure

The pore pressure in shale gas reservoirs is significantly different under different geological conditions and exploitation cases. Therefore, in this section simulation studies about the influence of gas pressures on gas transport in the fractured shale were performed. The REV of the shale with single fracture was selected as the geometry domain of the LBM simulation (Fig. 6), and the fracture fractal dimension was 2.3. The outlet gas pressure was set with five different values: 5 MPa, 10 MPa, 20 MPa, 30 MPa, and 40 MPa. The density, viscosity, and molecular mass of gas under different gas pressures were obtained by the Peace software. The other parameters and settings in the simulations kept consistent as in the previous simulations.

The 3D velocity distributions under different gas pressures are shown in Figure 16. Gas velocity in the crack and shale matrix decreased with increase in gas pressure, which cannot be explained by classical continuum fluid mechanics. Firstly, the gas rarefaction effect in micro-porous media plays a key role in gas flow at low gas pressure (Chen, Fang, et al., 2015). In this case, the collision of gas molecules with the pore/fracture wall becomes more frequent than internal gas molecules collision, resulting in the non-equilibrium distribution of gas molecules and the high slippage velocity near the gas–solid boundary (Wang et al., 2017). Secondly, higher viscosity can be induced by higher gas pressure, which leads to the increase in friction between the gas molecules and the pore/crack surface and to the decrease in the gas migration rate. On the other hand, the collision between gas molecules and the

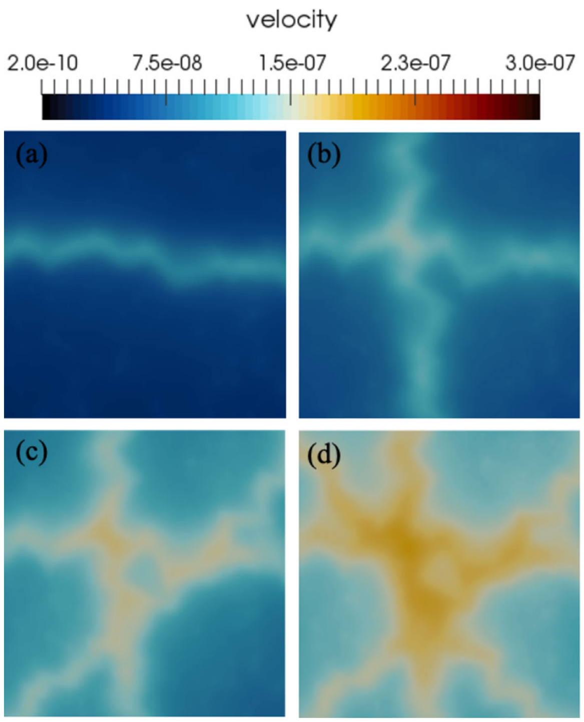

Figure 14. Velocity distribution in the middle slice of fractured shale with different crack numbers, (a)–(d): 1, 2, 3, 4.

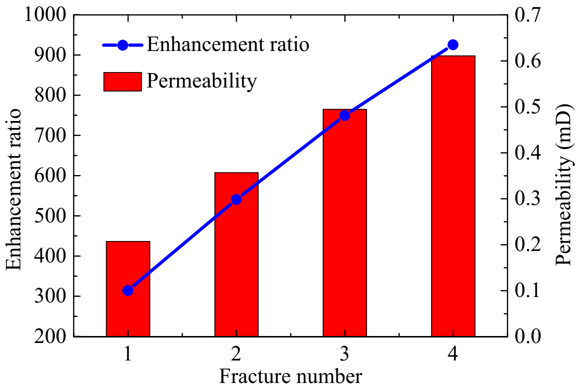

Figure 15. Effect of crack number on shale permeability.

pore/fracture wall surface becomes more violent with increasing gas pressure and further aggravates the loss of energy along the flow channel (Chen, Fang, et al., 2015).

The distributions of the stream-wise velocity magnitude in the shale matrix were extracted and shown in Figure 17. As shown, the gas velocity in the shale matrix was about one magnitude order lower compared with that in the fracture. However, similar to the gas velocity in the fracture, the gas velocity in the shale matrix also decreased obviously with increase in gas pressure. The peaks on the velocity profile became narrower. At low pressure, gas–solid interaction begins to dominate gas flow, and this unstable state results in increase of gas velocity in micro-porous media (Wang et al., 2017).

The permeability and permeability enhancement ratio of the fractured shale under different pore pressures are shown in Figure 18. As the gas velocity decreased with increasing gas pressure, the permeability of the fractured shale decreased monotonously with increase in gas pressure and the decrease was faster at low pressure. Its permeability reduced from 0.21 mD of 5 MPa to 0.09 mD of 40 MPa, with 57.14% reduction. The permeability enhancement ratio decreased from 314 of 5 MPa to 133 of 40 MPa. However, as shown in Figure 9, the permeability of the shale without the fracture decreased by 84.04% when the gas pressure increased from 1 MPa to 5 MPa, indicating that the presence of the fracture can weaken the influence of gas pressure on the permeability of the fractured shale. The fracture, as the main channel of gas flow, had a relatively large size, which resulted in reducing the influence of Klinkenberg's effect. However, the Klinkenberg's effect becomes serious in micro/nano pores of shale, especially at the low-pressure range. Therefore, the permeability of the fractured shale increased less than that of intact shale with decrease in gas pressure.

DISCUSSION

Base on the above results, the gas rarefaction effect induced by the gas pressure is serious in the fractured shale. From the study of Wang et al. (2017), the gas rarefaction effect is also highly dependent on the morphology of porous media. To evaluate quantitatively the effect of fracture morphology on the gas rarefaction effect, gas transport in the shale with different fracture structures was simulated under different gas pressures (5 MPa, 10 MPa, 20 MPa, 30 MPa, and 40 MPa). The permeability of the fractured shale as a function of gas pressure is shown in Figure 19.

As shown in Figure 19, similar to the results for permeability in section Gas Pressure above, at different fracture fractal dimensions and fracture number conditions, the permeability also increased monotonously with decreasing outlet gas pressure

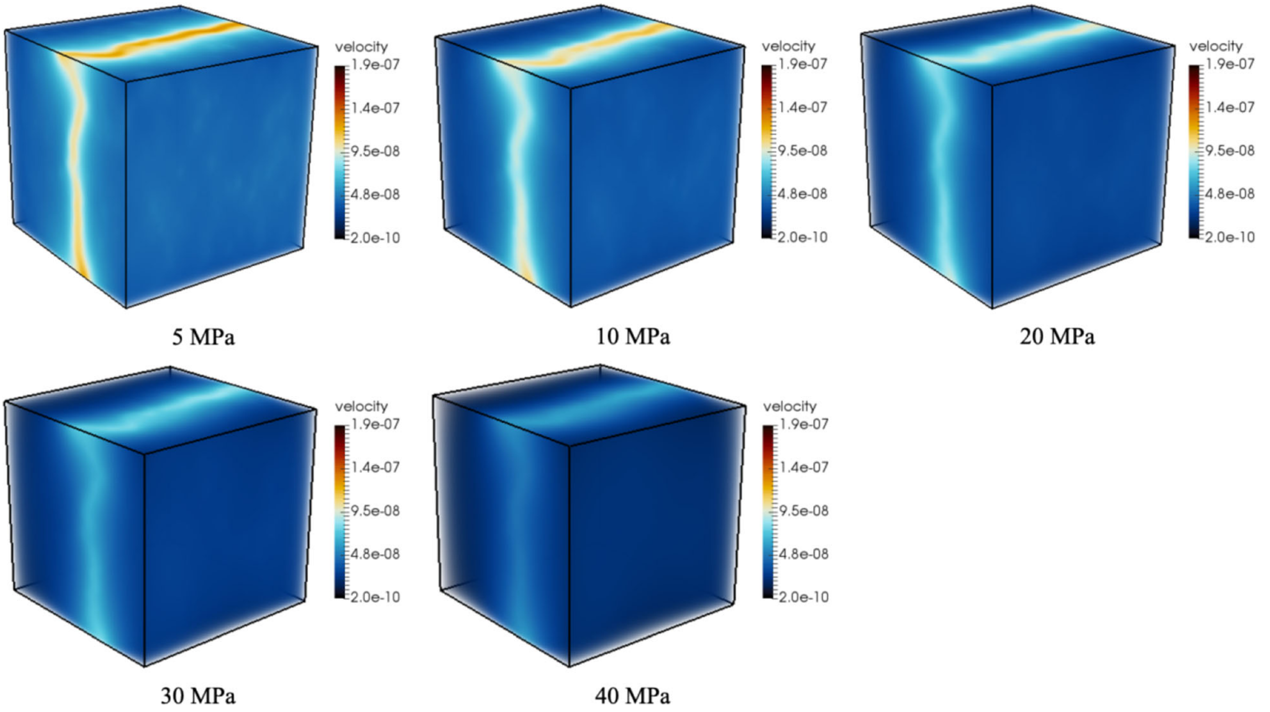

5 MPa

10 MPa

20 MPa

30 MPa

40 MPa

Figure 16. Effect of gas pressure on velocity distribution in fractured shale.

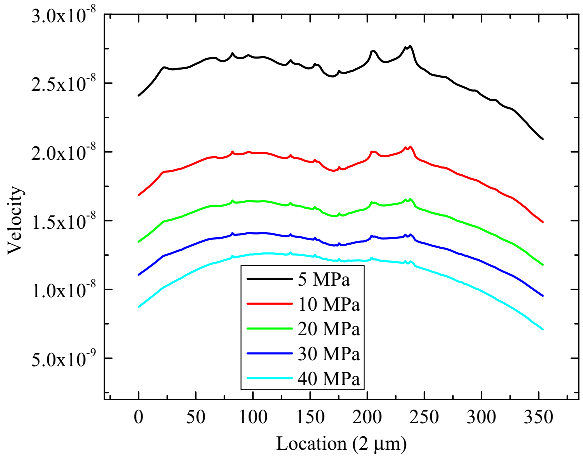

Figure 17. Velocity distribution in shale matrix under different gas pressures.

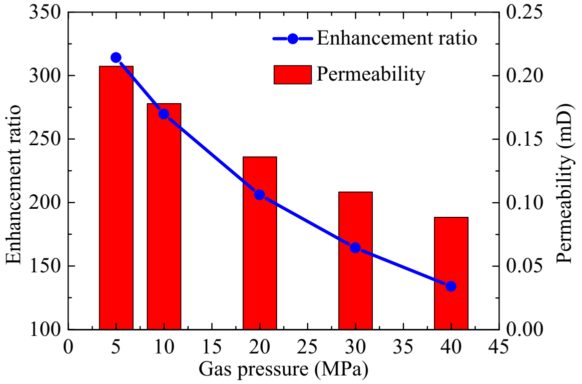

Figure 18. Effect of gas pressure on permeability of fractured shale.

and the increase was faster at the low gas pressure range. The result indicates that the permeability of the fractured shale was more sensitive at low-pressure condition. As gas pressure decreased, the gas–solid interaction became gradually significant for gas flow in pores/micro-fractures. At low pressure, high gas velocity was induced, which further gave rise to high gas permeability. In addition, the changes in permeability with gas pressure were more sensitive to the rougher fracture and the lower fracture numbers, which implies that the gas rarefaction effect became more significant in these conditions. For the shale with trough fracture or low fracture connectivity, the local bounded space size of the gas molecules was more easily close to the local MFP. As a result, the non-equilibrium status of the gas

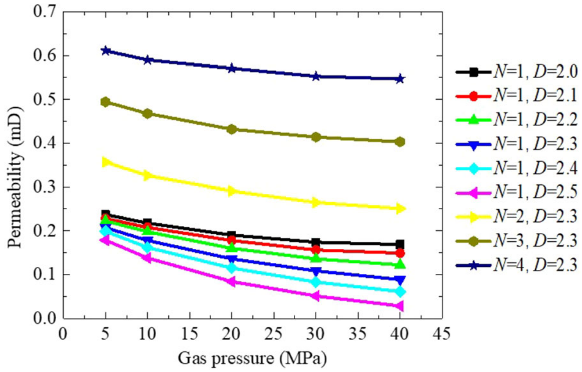

Figure 19. Changes in permeability of fractured shale with gas pressure.

molecules was easier to be induced in these conditions, which further gave rise to the relative larger difference in the gas slippage velocity between the different gas pressures.

CONCLUSIONS

In this study, a REV-scale LB model considering the Klinkenberg's effect and gas absorption was developed and applied to simulate gas flow in fractured shale. The 3D multi-scale structures of the fractured shale were reconstructed by the REV of the intact shale and the fracture fractal function. The REV-scale LB model was verified with analytical solution and experiment data. The effects of fracture morphology and gas rarefaction on the gas velocity distribution and permeability were simulated and analyzed. The conclusions reached are as follows. The fracture morphology in the fractured shale plays a prominent role in controlling gas flow behavior. Gas velocity and permeability in the fractured shale significantly decrease with increasing fracture fractal dimension due to the resistance to gas flow in rough fracture space. The permeability of the fractured shale had an obvious increase with increase in the complexity of the fracture network. The good connectivity of the fracture network generally contributes to forming local high-intensity velocity fields and increasing gas velocity in the shale matrix. The gas rarefaction effect had a significant influence on gas flow in the fractured shale. A large slippage velocity was easily induced due to the dominance of gas–solid interaction. The velocity slippage in the shale became more obvious, and the permeability of the fractured shale increased markedly at the low-pressure range, which indicates that the permeability of the fractured shale must be regarded as a dynamic shale reservoir parameter and updated based on the shale reservoir status. The gas flow behaviors of the fractured shale are more sensitive at low-pressure condition, and the gas rarefaction effect is more sensitive to the shale with highly rough fracture or low fracture connectivity.

ACKNOWLEDGMENTS

This work had been financially supported by the Open Fund of the State Key Laboratory of Coal Resources in Western China, Xi'an University of Science and Technology (SKLCRKF20-03), the Open Fund of the State Key Laboratory of Geohazard Prevention and Geoenvironment Protection, Chengdu University of Technology (SKLGP2020K004), and the China Postdoctoral Science Foundation (2020M673451).

REFERENCES

Ausloos, M., & Berman, D. H. (1985). A multivariate Weierstrass–Mandelbrot function. *Proceedings of the Royal Society of London Series A-Mathematical and Physical Sciences, 400*(1819), 331–350.

Bauer, M., & Rüde, U. (2018). *An improved lattice Boltzmann D3Q19 method based on an alternative equilibrium discretization.* arXiv:1803.04937v2.

Benamram, Z., Tarakanov, A., Nasrabadi, H., & Gildin, E. (2016). Field-wide flow simulation in fractured porous media within lattice Boltzmann framework. *Advances in Water Resources, 96,* 170–179.

Beskok, A., & Karniadakis, G. E. (1999). A model for flows in channels, pipes, and ducts at micro and nano scales. *Microscale Thermophysical Engineering, 3*(1), 43–77.

Cai, J. C., Lin, D. L., Singh, H., Wei, W., & Zhou, S. W. (2018). Shale gas transport model in 3D fractal porous media with variable pore T sizes. *Marine and Petroleum Geology, 98,* 437–447.

Carman, P. C. (1997). Fluid flow through granular beds. *Chemical Engineering Research and Design, 75,* S32–S48.

Chen, L., Fang, W. Z., Kang, Q. J., Hyman, J. D., Viswanathan, H. S., & Tao, W. Q. (2015a). Generalized lattice Boltzmann model for flow through tight porous media with Klinkenberg's effect. *Physical Review E, 91*(3), https://doi.org/10.1103/PhysRevE.91.033004.

Chen, L., Kang, Q. J., Dai, Z. X., Viswanathan, H. S., & Tao, W. Q. (2015b). Permeability prediction of shale matrix reconstructed using the elementary building block model. *Fuel, 160,* 346–356.

Chen, L., Kang, Q. J., Mu, Y. T., He, Y. L., & Tao, W. Q. (2014). A critical review of the pseudopotential multiphase lattice

Boltzmann model: Methods and applications. *International Journal of Heat and Mass Transfer, 76,* 210–236.

Chen, L., Zhang, L., Kang, Q. J., Viswanathan, H. S., Yao, J., & Tao, W. Q. (2015c). Nanoscale simulation of shale transport properties using the lattice Boltzmann method: permeability and diffusivity. *Scientific Reports, 5,* 8089. https://doi.org/10.1038/srep08089.

Civan, F. (2010). Effective correlation of apparent gas permeability in tight porous media. *Transport in Porous Media, 82*(2), 375–384.

Costanza-Robinson, M. S., Estabrook, B. D., & Fouhey, D. F. (2011). Representative elementary volume estimation for porosity, moisture saturation, and air–water interfacial areas in unsaturated porous media: Data quality implications. *Water Resources Research, 47,* W07513. https://doi.org/10.1029/2010WR009655.

Darabi, H., Ettehad, A., Javadpour, F., & Sepehrnoori, K. (2012). Gas flow in ultra-tight shale strata. *Journal of Fluid Mechanics, 710,* 641–658.

Dewers, T. A., Heath, J., Ewy, R., & Duranti, L. (2012). Three-dimensional pore networks and transport properties of a shale gas formation determined from focused ion beam serial imaging. *International Journal of Oil Gas and Coal Technology, 5*(2–3), 229–248.

Gao, J. F., Xing, H. L., Tian, Z. W., & Muhlhaus, H. (2014). Lattice Boltzmann modeling and evaluation of fluid flow in heterogeneous porous media involving multiple matrix constituents. *Computers & Geosciences, 62,* 198–207.

Guo, C. H., Xu, J. C., Wei, M. Z., & Jiang, R. Z. (2015). Experimental study and numerical simulation of hydraulic fracturing tight sandstone reservoirs. *Fuel, 159,* 334–344.

Guo, Z. L., & Zhao, T. S. (2002). Lattice Boltzmann model for incompressible flows through porous media. *Physical Review E, 66*(3), https://doi.org/10.1103/PhysRevE.66.036304.

Guo, Z. L., Zheng, C. G., & Shi, B. C. (2002). Discrete lattice effects on the forcing term in the lattice Boltzmann method. *Physical Review E, 65*(4), https://doi.org/10.1103/PhysRevE.65.046308.

Heid, J. G., McMahon, J. J., Nielsen, R. F., & Yuster, S. T. (1950). *Study of the permeability of rocks to homogeneous fluids.* Paper presented at the Drilling and Production Practice, New York, New York, USA, 1 January.

Hou, P., Gao, F., Gao, Y. N., Yang, Y. G., & Cai, C. Z. (2018). Changes in breakdown pressure and fracture morphology of sandstone induced by nitrogen gas fracturing with different pore pressure distributions. *International Journal of Rock Mechanics and Mining Sciences, 109,* 84–90.

Hou, P., Gao, F., He, J., Liu, J., Xue, Y., & Zhang, Z. P. (2020). Shale gas transport mechanisms in inorganic and organic pores based on lattice Boltzmann simulation. *Energy Reports, 6,* 2641–2650.

Hou, P., Gao, F., Ju, Y., Yang, Y. G., Gao, Y. N., & Liu, J. (2017a). Effect of water and nitrogen fracturing fluids on initiation and extension of fracture in hydraulic fracturing of porous rock. *Journal of Natural Gas Science and Engineering, 45,* 38–52.

Hou, P., Ju, Y., Cai, C. Z., Gao, L., & Su, S. J. (2017b). Lattice Boltzmann simulation of fluid flow induced by thermal effect in heterogeneity porous media. *Thermal Science, 21,* S193–S200.

Huang, J. C., Hu, J. H., Zeng, W. T., & Zhang, Y. (2019). Investigation of a critical choke during hydraulic-fracture flowback for a tight sandstone gas reservoir. *Journal of Geophysics and Engineering, 16*(6), 1178–1190.

Javadpour, F., Fisher, D., & Unsworth, M. (2007). Nanoscale gas flow in shale gas sediments. *Journal of Canadian Petroleum Technology, 46*(10), 55–61.

Ji, L. L., Lin, M., Cao, G. H., & Jiang, W. B. (2019). A multiscale reconstructing method for shale based on SEM image and experiment data. *Journal of Petroleum Science and Engineering, 179,* 586–599.

Jia, Y. Z., Lu, Y. Y., Elsworth, D., Fang, Y., & Tang, J. R. (2018). Surface characteristics and permeability enhancement of shale fractures due to water and supercritical carbon dioxide fracturing. *Journal of Petroleum Science and Engineering, 165,* 284–297.

Jiang, C. B., Niu, B. W., Yin, G. Z., Zhang, D. M., Tang, Y., & Wang, P. (2019). CT-based 3D reconstruction of the geometry and propagation of hydraulic fracturing in shale. *Journal of Petroleum Science and Engineering, 179,* 899–911.

Ju, Y., Zhang, Q. G., Zheng, J. T., Chang, C., & Xie, H. P. (2017). Fractal model and Lattice Boltzmann method for characterization of non-Darcy flow in rough fractures. *Scientific Reports, 7,* 41380. https://doi.org/10.1038/srep41380.

Klinkenberg, L. J. (1941). The permeability of porous media to liquids and gases. *Socar Proceedings, 2*(2), 200–213.

Lei, Y. H., Luo, X. R., Wang, X. Z., Zhang, L. X., Jiang, C. F., Yang, W., et al. (2015). Characteristics of silty laminae in Zhangjiatan Shale of southeastern Ordos Basin, China: Implications for shale gas formation. *AAPG Bulletin, 99*(4), 661–687.

Li, J. H., Li, B. B., Wang, Z. H., Ren, C. C., Yang, K., & Chen, S. (2020). An anisotropic permeability model for shale gas recovery considering slippage effect and embedded proppants. *Natural Resources Research, 29,* 3319–3333.

Li, X., Feng, Z. J., Han, G., Elsworth, D., Marone, C., Saffer, D., et al. (2016a). Breakdown pressure and fracture surface morphology of hydraulic fracturing in shale with H_2O, CO_2 and N_2. *Geomechanics and Geophysics for Geo-Energy and Geo-Resources, 2*(2), 63–76.

Li, Z. Z., Min, T., Kang, Q. J., He, Y. L., & Tao, W. Q. (2016b). Investigation of methane adsorption and its effect on gas transport in shale matrix through microscale and mesoscale simulations. *International Journal of Heat and Mass Transfer, 98,* 675–686.

Liu, S. X., Wang, Z. X., & Zhang, L. Y. (2018). Experimental study on the cracking process of layered shale using X-ray microCT. *Energy Exploration & Exploitation, 36*(2), 297–313.

Miao, T. J., Yang, S. S., Long, Z. C., & Yu, B. M. (2015). Fractal analysis of permeability of dual-porosity media embedded with random fractures. *International Journal of Heat and Mass Transfer, 88,* 814–821.

Nelson, P. H. (2009). Pore-throat sizes in sandstones, tight sandstones, and shales. *AAPG Bulletin, 93*(3), 329–340.

Nithiarasu, P., Seetharamu, K. N., & Sundararajan, T. (1997). Natural convective heat transfer in a fluid saturated variable porosity medium. *International Journal of Heat and Mass Transfer, 40*(16), 3955–3967.

Ren, J. J., Zheng, Q., Guo, P., & Zhao, C. L. (2019). Lattice Boltzmann model for gas flow through tight porous media with multiple mechanisms. *Entropy, 21*(2), 133. https://doi.org/10.3390/e21020133.

Saif, T., Lin, Q. Y., Butcher, A. R., Bijeljic, B., & Blunt, M. J. (2017). Multi-scale multi-dimensional microstructure imaging of oil shale pyrolysis using X-ray micro-tomography, automated ultra-high resolution SEM, MAPS Mineralogy and FIB-SEM. *Applied Energy, 202,* 628–647.

Shen, Y. H., Pang, Y., Shen, Z. Q., Tian, Y. Y., & Ge, H. K. (2018). Multiparameter analysis of gas transport phenomena in shale gas reservoirs: Apparent permeability characterization. *Scientific Reports*. https://doi.org/10.1038/s41598-018-20949-2.

Tahmasebi, P., Javadpour, F., Sahimi, M., & Piri, M. (2016). Multiscale study for stochastic characterization of shale samples. *Advances in Water Resources, 89,* 91–103.

Tang, X. L., Jiang, Z. X., Jiang, S., & Li, Z. (2016). Heterogeneous nanoporosity of the Silurian Longmaxi Formation shale gas reservoir in the Sichuan Basin using the QEMSCAN, FIB-

SEM, and nano-CT methods. *Marine and Petroleum Geology, 78,* 99–109.

Wang, J. J., Kang, Q. J., Wang, Y. Z., Pawar, R., & Rahman, S. S. (2017). Simulation of gas flow in micro-porous media with the regularized lattice Boltzmann method. *Fuel*, *205*, 232–246. https://doi.org/10.1016/j.fuel.2017.05.080.

Wang, Y., Wang, L. H., Wang, J. Q., Jiang, Z., Wang, C. C., Fu, Y. N., et al. (2019). Multiscale characterization of three-dimensional pore structures in a shale gas reservoir: A case study of the Longmaxi shale in Sichuan basin, China. *Journal of Natural Gas Science and Engineering, 66,* 207–216.

Wu, J. G., Yuan, Y., Niu, S. Y., Wei, X. F., & Yang, J. J. (2020). Multiscale characterization of pore structure and connectivity of Wufeng–Longmaxi shale in Sichuan Basin, China. *Marine and Petroleum Geology, 120,*. https://doi.org/10.1016/j.marpetgeo.2020.104514.

Wu, T. H., Li, X., Zhao, J. L., & Zhang, D. X. (2017). Multiscale pore structure and its effect on gas transport in organic-rich shale. *Water Resources Research, 53*(7), 5438–5450.

Zhang, G. L., Ranjith, P. G., Perera, M. S. A., Lu, Y. Y., & Choi, X. (2019). Quantitative analysis of micro-structural changes in a bituminous coal after exposure to supercritical CO_2 and water. *Natural Resource Research, 28,* 1639–1660.